CHAPTER

7

Bacteria-Inspired Microrobots

Kathrin E. Peyer*, Arthur W. Mahoney†, Li Zhang*, Jake J. Abbott‡, and Bradley J. Nelson*

*Institute of Robotics and Intelligent Systems, ETH Zurich, 8092 Zurich, Switzerland

†School of Computing, University of Utah, Salt Lake City, Utah 84112, USA

‡Department of Mechanical Engineering, University of Utah, Salt Lake City, Utah 84112, USA

Microbiorobotics. DOI: 10.1016/B978-1-4557-7891-1.00007-4

7.1 Introduction

Artificial bacterial microrobots are swimming microrobots that mimic the propulsion mechanism of bacteria, which use the rotation of helical filaments for motion generation. The potential applications for bacteria-inspired microrobots are diverse, ranging from diagnostic and therapeutic tasks in vivo to probing, analyzing, and transporting microobjects in biology, to fluidic applications in lab-on-a-chip devices. The development of microrobotics systems envelops numerous design challenges, including the fabrication of microagents, providing wireless power and finding locomotion methods suitable for the low Reynolds (*Re*) number flow regime in which they exist, to name just a few (see Fig. 7.1).

This chapter will first take the reader through an introduction into the fluid mechanics at the microscale in general and present common terms and modeling methods. The following section covers the description of how bacteria swim, how

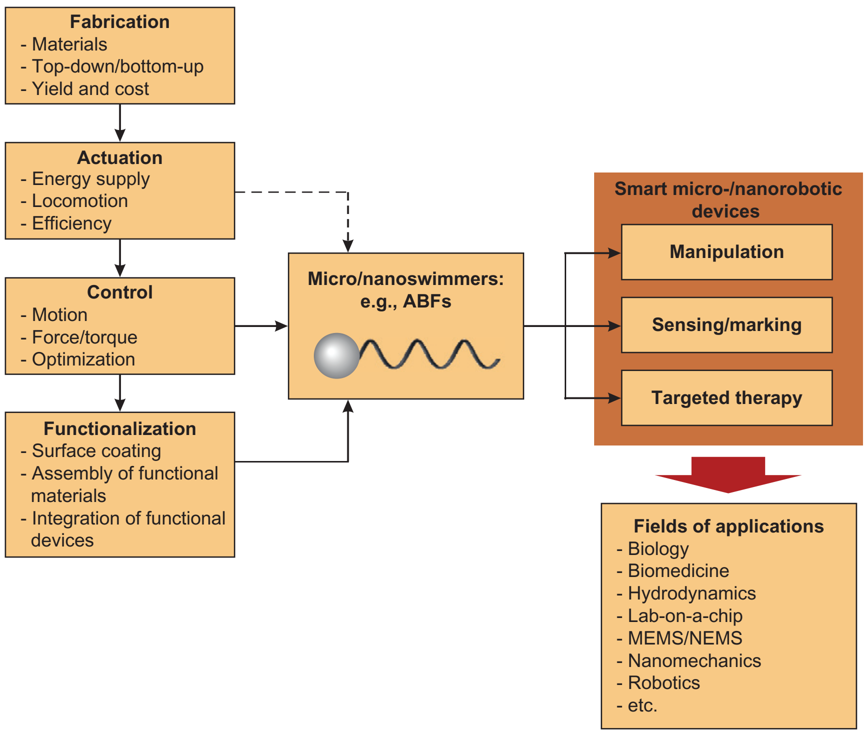

FIGURE 7.1

A road map for helical swimming microrobots we call artificial bacterial flagella (ABFs). Reproduced with permission from Ref. [1], The Royal Society of Chemistry.

we can model their motion, and how the fabrication of similar-sized bacterial microrobots has been achieved in recent years. Next, we address the challenge of power supply for bacteria-inspired microrobots and the use of rotating magnetic fields for actuation and steering. Recent success in actuating and steering these microrobots has allowed the investigation of their swimming behavior. Interestingly, the effects of boundaries on ABFs can be directly compared to the findings of how swimming bacteria are affected. A number of phenomena, including frequency dependent swimming behaviors and gravitational influences, are unique to bacterial robots and deserve special attention. The last section summarizes the success in utilizing bacterial microrobots for manipulation tasks thus far and discusses future challenges.

7.2 Fluid mechanics at low Reynolds numbers

Humans live in a macroscopic world, and we have developed an intuition for the world around us and expect, for example, that turbulence occurs when fast flows, either gas or liquid, hit a blunt obstacle. As we enter the microscopic world, even though the laws of physics remain the same, the relative importance of forces and effects changes drastically. When engineering microrobotic systems, it is important to learn a new intuition about the behavior of physics at the microscale. The first section of this chapter gives an insight into fluid mechanics at low Reynolds numbers and methods available to model laminar flows and the motion of microswimmers.

7.2.1 The Reynolds number

In the field of fluid mechanics, the most commonly discussed one is the dimensionless Reynolds number (Re), because it plays an important role in characterizing the flow regime, such as laminar or turbulent flow, and it is used to define the transition from one flow regime to the other. It is defined as

$$Re = \frac{U_0 L \rho}{\eta} \sim \frac{\text{inertial forces}}{\text{viscous forces}} \tag{7.1}$$

where U_0 and L are the free-stream velocity and characteristic length, respectively, and ρ and η are the density and dynamic viscosity of the fluid. The Reynolds number is a measure of the ratio of inertial to viscous forces, and for $Re \ll 1$, the flow becomes very "viscous," e.g., like honey, and is called *creeping* or *Stokes* flow. In addition to the "traditional" Reynolds number, a "rotational" Reynolds number Re_r can be defined as

$$Re_r = \frac{\omega L^2 \rho}{\eta} \tag{7.2}$$

where ω is the rotational speed. Both Re and Re_r have to be considered when determining the flow regime.

Micro-organisms as well as the microrobots discussed in this chapter swim in a low *Re* number regime simply because of their size and speed. The Stokes equation, which describes the flow, is given by

$$\nabla p = \eta \nabla^2 \boldsymbol{U} + \boldsymbol{f} \tag{7.3}$$

where $\boldsymbol{U}$ is the velocity vector field, p is the pressure scalar field, η is the dynamic viscosity, and $\boldsymbol{f}$ is the body forces acting on the fluid. Equation (7.3) is a simplification of the Navier-Stokes equation and is correct only for $Re = 0$, but can be used as an approximate solution for $Re \ll 1$. Three important properties of the Stokes' flow shall be addressed separately. The first one is the fact that inertia is negligible; this can be seen directly from the Reynolds number in Eq. (7.1). The second characteristic is the time-invariance, and the third one is the linearity of the Stokes' equation. These two latter properties can be recognized from the Stokes' Eq. (7.3).

7.2.1.1 On the lack of inertia

The negligible effect of inertia in Stokes' flow is best demonstrated with a case study of a microsphere in water. A sphere with a radius of $R = 1\,\mu\text{m}$ that is pulled at a velocity of $U_0 = 10\,\mu\text{m/s}$ has a Reynolds number of $Re \approx 10^{-5}$ assuming a density and dynamic viscosity of water of $\rho_w \approx 10^3\,\text{kg/m}^3$ and $\eta \approx 10^{-3}\,\text{Pa}\cdot\text{s}$, respectively. Without external force, the sphere coasts for a distance d before it comes to a halt. The coasting distance can be calculated by solving the differential equation $m\dot{U}(t) + \psi_u U(t) = 0$, where $\psi_u = 6\pi\eta R$ is the translational drag coefficient of a sphere in Stokes flow. For a microsphere with density $\rho_s \approx 10^4\,\text{kg/m}^3$, the coasting distance is only $d \approx 2\,\text{Å}$, and it is apparent that inertial effects are indeed very small. The coasting time is computed to be around $t \approx 2\,\mu\text{s}$. This suggests that the acceleration and deceleration times are very short and are also generally considered negligible. Hence, a microswimmer reaches the steady-state motion almost instantaneously.

7.2.1.2 On the time-reversibility

The time-reversibility can be recognized from the lack of a time derivative of the flow field in Eq. (7.3), and it has an important impact when microswimmers want to propel themselves. At high Reynolds numbers, it is possible to generate thrust by moving a stiff oar up and down at different speeds. The momentum of the water is different when being moved fast (down-beat of the oar) or slowly (up-beat of the oar). In creeping flow conditions, the up and down movement of a stiff oar does not yield a net propulsion but simply a back and forth movement because the flow is almost perfectly reversible. This is referred to as the *scallop theorem* [2]. This reversibility dictates the propulsion methods that can be employed by microscopic swimmers. In order to produce a net displacement, a microswimmer has to go through a non-reciprocal motion.[1] This concept can be demonstrated with a theoretical three-link swimmer

[1] The *scallop theorem* is only valid in a Newtonian liquid. It has been demonstrated that reciprocal motion in a Non-Newtonian liquid can create a net propulsion [3].

depicted in Fig. 7.2. The two hinges offer two degrees of freedom (2DOF), and the swimmer can go through a series of angle configuration. The non-reciprocal series of configurations *ABCDA* (see Fig. 7.2A) results in a net displacement after one cycle. The series of configurations *ABCBA* (Fig. 7.2B) on the other hand is reciprocal, and no net displacement is achieved after one cycle [2]. The continuous rotation of a helix is one such non-reciprocal motion and is used by bacteria, such as *Escherichia coli*, as a propulsion method. Helical swimming is described in more detail in Section 7.3.1.

7.2.1.3 On the linearity

The linearity of the Stokes' equations plays an important role for the modeling of fluid mechanics. In particular, it allows the superposition of singularity solutions; a method that is the basis for most means used to solve the Stokes' equations. This method is further explained in Section 7.2.1. A very useful property for the modeling of rigid body motions can be extracted from the linearity of the Stokes flow, which is that the relationships between the body's velocity $\boldsymbol{U}$, rotational speed $\boldsymbol{\Omega}$, external force $\boldsymbol{F}$, and external torque $\boldsymbol{T}$ are related linearly and can be represented by a matrix equation of the following form [4]:

$$\begin{pmatrix} \boldsymbol{F} \\ \boldsymbol{T} \end{pmatrix} = \begin{pmatrix} A & B \\ B^T & C \end{pmatrix} \begin{pmatrix} \boldsymbol{U} \\ \boldsymbol{\Omega} \end{pmatrix} \tag{7.4}$$

A, B, and C are each 3×3 matrices. For a sphere of radius R, the entries are $A = \mathbf{I} \cdot 6\pi\eta R$, $B = 0$, and $C = \mathbf{I} \cdot 8\pi\eta R^3$. There are bodies with no mirror symmetry planes, e.g., chiral bodies, that have a matrix with $B \neq 0$. This means that a linear force can drive a rotational motion or, conversely, an external torque can drive a linear motion.

7.2.2 Modeling Stokes flow

The modeling of Stokes flow around stationary or moving objects has been a research topic for many decades [4–8]. The linearity of the Stokes equation allows for either

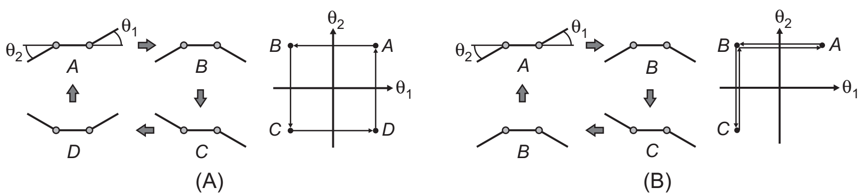

FIGURE 7.2

Theoretical three-link swimmer as described in Ref. [2]. The two hinges can go through a non-reciprocal (A) or reciprocal (B) configuration of angles. (A) The non-reciprocal series of angle configurations *ABCDA* creates a net displacement after a whole cycle. (B) The reciprocal series of configurations *ABCBA* leads to a back and forth motion only.

an analytical treatment or numerical approaches with a lower computational cost than modeling high Reynolds number flows. Researchers from a variety of fields, such as fluid mechanics, mathematics, biology, and recently microrobotics, have interest in low Reynolds number modeling and, accordingly, a multitude of publications are available. This section is for the benefit of readers with little background in low Reynolds number modeling to introduce them to commonly used terms and methods.

As the Stokes equation is linear, the superposition of singular solutions is possible, and it is often referred to as the method of fundamental solutions (MFSs) or simply the singularity method. The superposition of singularities is the basis for all the other methods and is therefore presented first. An introduction to the boundary element method (BEM), the slender body theory (SBT), and resistive force theory (RFT) follow.

7.2.2.1 Method of fundamental solutions (MFS)

For special types of external forces, the Stokes Eq. (7.3) can be solved analytically. One such force is a singular point force $\boldsymbol{f_s} = \delta(\boldsymbol{x} - \boldsymbol{x_s})\boldsymbol{b}$, where δ is the Dirac delta. This force acts on the fluid at the position $\boldsymbol{x_s}$, and $\boldsymbol{b}$ constitutes the direction and magnitude of the force. The resulting flow due to the presence of this force can be computed analytically by solving the equation

$$-\nabla p + \eta \nabla^2 \boldsymbol{U} = -\delta(\boldsymbol{x} - \boldsymbol{x_s})\boldsymbol{b}. \tag{7.5}$$

The resulting flow field velocity $\boldsymbol{u}(\boldsymbol{x})$ is [9]

$$u_i(\boldsymbol{x}) = S_{ij}(\boldsymbol{x},\boldsymbol{x_s}) \cdot b_j, \qquad S_{ij}(\hat{\boldsymbol{x}}) = \frac{1}{8\pi\eta}\left(\frac{\delta_{ij}}{r} + \frac{\hat{x}_i \hat{x}_j}{r^3}\right) \tag{7.6}$$

where $\hat{\boldsymbol{x}} = \boldsymbol{x} - \boldsymbol{x_s}$ and $r = |\hat{\boldsymbol{x}}|$. Similarly, simple expressions can be found for the pressure field and stress tensor [9]. S_{ij} is called a *stokeslet* or the *Oseen–Burgers tensor* and is the most important *fundamental* or *singularity* solution of the Stokes' flow. The Stokes equation can be solved for different geometries by superposition of these singularity solutions. This often involves a two-step approach, where the singularities are first distributed and their strength determined such that the boundary conditions are fulfilled, and subsequently the velocities at discrete field points of interest are calculated using Eq. (7.6). The *stokeslet* is one of the most commonly used singularities, though other singularities have been successfully employed [10].

7.2.2.2 Boundary element method (BEM)

The boundary element method (BEM) uses a different approach to solve the Stokes flow around an arbitrary geometric body. Instead of directly superposing singularities, an integral equation over the surface of a body is found:

$$u_j(\boldsymbol{x_s}) = \int_S u_i(\boldsymbol{x}) T_{ijk}(\boldsymbol{x},\boldsymbol{x_s}) n_k(\boldsymbol{x}) \mathrm{d}S(\boldsymbol{x}) - \int_S S_{ji}(\boldsymbol{x_s},\boldsymbol{x}) f_i(\boldsymbol{x}) \mathrm{d}S(\boldsymbol{x}) \tag{7.7}$$

by using the *Lorentz reciprocal theorem* [9]. S_{ij} is the *stokeslet*, $T_{ijk}(\hat{\boldsymbol{x}}) = -3\hat{x}_i\hat{x}_j\hat{x}_k/4\pi\eta r^5$, and $\boldsymbol{f} = \sigma\boldsymbol{n}$ is the modified boundary traction. Details on the derivation and the application of this method can be found in the literature [7, 9, 11–16]. The drag force on a body, a common parameter of interest, is contained in the boundary traction force $\boldsymbol{f}$ introduced in this method.

Equation (7.7) is not valid at the point of the singularity $\boldsymbol{x_s}$ and special integration methods have to be used to solve Eq. (7.7) over the surface that includes the singularity. One way to avoid this problem is by using the method of *regularized stokeslets* established by Cortez [17, 18]. Instead of solving the Stokes' equation for a point force (see Eq. (7.5)), which is singular at the point x_s, the force is applied over a spreading function distribution $\Phi_\epsilon(\boldsymbol{x} - \boldsymbol{x}_s)$ with no singular point. The Stokes' equation that needs to be solved has the form

$$-\nabla p + \eta\nabla^2\boldsymbol{U} = -\Phi_\epsilon(\boldsymbol{x} - \boldsymbol{x}_s)\boldsymbol{f_s} \tag{7.8}$$

where Φ_ϵ is a *cutoff* function that is not singular at $\boldsymbol{x_s}$ and with the property $\int_\infty^{-\infty}\Phi_\epsilon(\boldsymbol{x})\mathrm{d}\boldsymbol{x} = 1$. Instead of finding the "traditional" fundamental solution, i.e., the *stokeslet* S_{ij}, the new *regularized stokeslet* is found.

$$S_{ij}^\epsilon(\boldsymbol{x}, \boldsymbol{x_s}) = \delta ij\frac{r^2 + 2\epsilon^2}{(r^2 + \epsilon^2)^{3/2}} + \frac{(x_i - x_{s,i})(x_j - x_{s,j})}{(r^2 + \epsilon^2)^{3/2}} \tag{7.9}$$

A parameter ϵ is used to tune the spreading of the function Φ_ϵ, and for ϵ approaching zero, the *regularized stokeslet* S_{ij}^ϵ goes toward $S_{ij}/(8\pi\eta)$. Regularized expressions are also derived for the pressure and the stress tensor and are listed in Refs. [17, 18]. When the boundary integral is formulated with the *regularized stokeslets*, a numerical solution can be found using quadrature rules for the surface integrals, without having to treat improper integrals that contain singularities.

7.2.2.3 Slender body theory

Generally, the influence of a body on the fluid can be modeled by distributing singularity solutions over its surface as described above. With the slender body approximation, the singularities are distributed only along the centerline, which decreases the complexity of the calculation. In order that the slender body approximation is valid, the width of the body should be much smaller than the length $w \ll L$. With the decreased complexity, even analytical treatment is possible and the solution for straight and curved slender bodies can be found [4, 19–22]. In recent years, numerical methods have been used to solve the singularity distribution for arbitrary (slender) shapes, such as rotating helices [23] or beating cilia [24].

7.2.2.4 Resistive force theory

The resistive force theory is somewhat different to the methods described previously. It is not intended to calculate the flow profile but simply the force–velocity relationship between a body and its surrounding liquid. This relationship is described with a drag coefficient $F = -\xi_{\text{drag}} \cdot u$. The derivation is often based on the singularity methods and a variety of authors have published coefficients for slender bodies using the slender body theory [22, 25, 26]. Despite the fact that these coefficients are only approximations, they are very powerful at deriving analytical or numerical models at a low computational cost and give good results with regard to qualitative behavior. A compilation of drag coefficients ξ_i for slender bodies is presented in Table 7.1, and the parameters are depicted in Fig. 7.3. The drag force can be computed as $F_i = -\int \xi_i \mathrm{d}s \cdot u_i$. In the case of a helical or undulating rod with a wavelength λ, the drag coefficients have to be understood as coefficients for a slender cylinder, with circular cross section $2r$, of length $\mathrm{d}s$, where $\mathrm{d}s$ has to be integrated along the centerline of the curved rod (see Fig. 7.3C). The coordinate system ξ_i corresponds to the local coordinate system of the cylinder. This needs to be considered when integrating along the helical curve.

Table 7.1 Drag Coefficients Per Unit Length for Slender Bodies. The Letters (A)–(C) Refer to Fig. 7.3, Where the Geometrical Parameters are Depicted. The Drag Force is $F_i = -\int \xi_i \mathrm{d}s \cdot u_i$.

	ξ_x	ξ_y	ξ_z	**Author**
(A)	$\frac{2\pi\eta}{\ln\left(\frac{2l}{r}\right)-0.5}$	$\frac{4\pi\eta}{\ln\left(\frac{2l}{r}\right)+0.5}$	$=\xi_y$	Chwang and Wu [25]
(B)	$\frac{2\pi\eta}{\ln\left(\frac{2l}{r}\right)-0.807}$	$\frac{4\pi\eta}{\ln\left(\frac{2l}{r}\right)+0.193}$	$=\xi_y$	Cox [22]
(C)	$\frac{2\pi\eta}{\ln\left(\frac{2\lambda}{r}\right)-2.9}$	$\frac{4\pi\eta}{\ln\left(\frac{2\lambda}{r}\right)-1.9}$	$=\xi_y$	Lighthill [26]

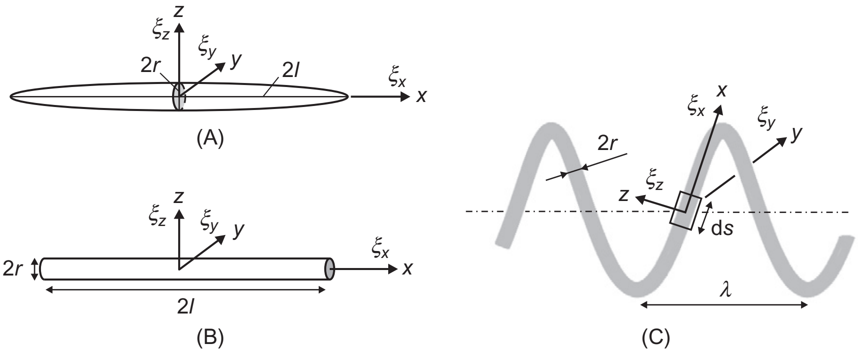

FIGURE 7.3

The parameters for calculating the drag coefficients for slender bodies in Table 7.1. (A) Ellipse with a circular cross section; (B) cylinder with a circular cross section; (C) cylinder element with a circular cross section of an undulating rod with a wavelength λ.

7.3 Bacterial swimming

7.3.1 Bacteria swim by rotating helical filaments

In nature, micro-organisms have found numerous ways to propel themselves, including beating flexible flagella and cilia [2]. Bacterial swimmers, such as the extensively researched *E. coli* bacterium, use a molecular motor to rotate helically shaped flagella [27, 28]. The continuous rotation of a helix is a non-reciprocal motion and, therefore, perfectly suited for low Reynolds number navigation. The rotation of the flagella has to be balanced by a counter-rotation of the bacterium's body (see Fig. 7.4). The rotation of the body does not add to the forward propulsion of the swimmer; indeed, the opposite is true as the bacterium has to use energy to overcome the additional drag caused by the rotation of its body. In order to understand how the rotation of a helix creates a forward movement, we can look at a simplified RFT-based swimming model.

7.3.2 Modeling helical swimming

In order to produce a displacement with a helical filament, two conditions have to be fulfilled. First, a drag anisotropy on the slender filament has to be present. From the drag coefficients listed in Table 7.1, it is apparent that this is indeed the case for a slender cylindrical rod. The ratio of drag force on a cylinder moving perpendicular and on a cylinder moving parallel to its axis is approximately two (in fact it is less). For example, if we look at a slender cylinder that has an oblique angle to the gravitational pull (see Fig. 7.5A), the drag anisotropy of the cylinder causes a settling velocity with components both in vertical and horizontal directions. The second condition is that the cylinder has to go through a non-reciprocal motion, which is the case for each section of the rotating helical filament.

In Section 7.2.1, it was shown that the motion of a rigid object can be presented with a matrix Eq. (7.4). Using RFT, which provides us with a force–velocity relationship for slender cylinders, we can find the matrix entries for a helical geometry by integrating along the length of the filament. A 3D-motion model and the detailed derivation of this can be found in Ref. [29]. For the purpose of understanding helical propulsion within the scope of this chapter, a simplified model will suffice. It was Purcell who showed that helical propulsion could be approximated by using a 2×2 matrix to relate the forward velocity u, rotational speed ω, force F, and torque T

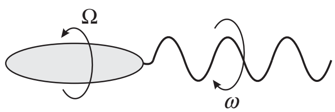

FIGURE 7.4

A bacterium rotates its helical tail at a frequency of ω. To achieve a force equilibrium on the bacterium, the head has to counter-rotate with a (lower) frequency Ω.

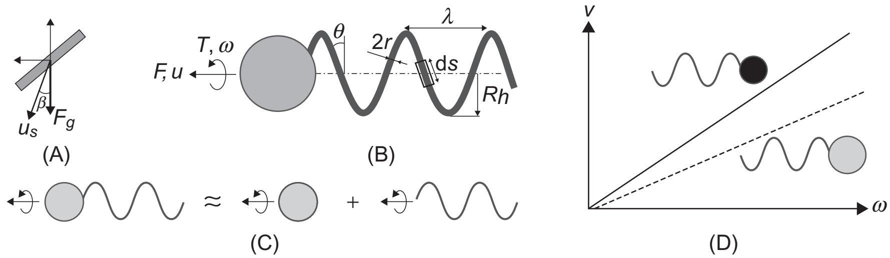

FIGURE 7.5

(A) A slender cylinder is pulled downward by gravitational forces at an oblique angle. The resulting settling velocity is tilted by an angle β. (B) 1D model of helical swimming relates the velocity u, rotational speed ω, force F, and torque T. The helicity angle is θ, λ is the pitch, R_h is the radius of the helix, and R_b is the radius of the spherical body. (C) Assuming that the head does not influence the flow around the tail, the solution for the motion of the entire swimmer is the sum of the solutions for the helical tail and the spherical body. (D) The forward velocity of the helical swimmer is linearly dependent on the rotational frequency. A large head creates more drag and decreases the slope of the frequency–velocity relationship.

around the helical axis [2, 30] (see Fig. 7.5B).

$$\begin{pmatrix} F \\ T \end{pmatrix} = \begin{pmatrix} a & b \\ b & c \end{pmatrix} \begin{pmatrix} u \\ \omega \end{pmatrix} \tag{7.10}$$

Purcell called the matrix in Eq. (7.10) the "propulsion" matrix, and its coefficients a, b, and c are scalars. They can be found by establishing the force and torque equilibrium in the direction of the helical axis

$$a = 2\pi n R_h \left(\frac{\xi_{\parallel} \sin^2\theta + \xi_{\perp} \cos^2\theta}{\cos\theta} \right)$$

$$b = 2\pi n R_h^2 (\xi_{\parallel} - \xi_{\perp}) \sin\theta$$

$$c = 2\pi n R_h^3 \left(\frac{\xi_{\parallel} \cos^2\theta + \xi_{\perp} \sin^2\theta}{\cos\theta} \right)$$

$\xi_{\parallel}$ and $\xi_{\perp}$ correspond to the drag coefficients ξ_x and $\xi_y = \xi_z$, respectively, listed in Table 7.1. This result is valid for an integer n number of turns. The helix parameters λ, θ, and R_h are defined in Fig. 7.5B. F and T are an external force and torque, respectively, one of which has to be present to move the helical body.

A simple approach to model the influence of the swimmer's body is to approximate it by the motion of a sphere. The propulsion matrix for a sphere is simple as it has no drag anisotropy and the resistance to translational and rotational motions, $\psi_v = 6\pi\eta R_b$ and $\psi_\omega = 8\pi\eta R_b^3$, respectively, is the same in all directions.

$$\begin{pmatrix} F \\ T \end{pmatrix} = \begin{pmatrix} \psi_v & 0 \\ 0 & \psi_\omega \end{pmatrix} \begin{pmatrix} u \\ \omega \end{pmatrix} \tag{7.11}$$

In the case of a bacterium, the head would rotate at a lower speed and in the opposite direction to the helical tail. The microrobots discussed here do not have this relative movement between their body and helical tail (see next section on Fabrication methods). Instead, the body and tail form one rigid body and the propulsion matrices of the body and tail can, under the simplifying assumption that the flows around each part do not influence each other, be combined into one model:

$$\begin{pmatrix} F \\ T \end{pmatrix} = \begin{pmatrix} \alpha & b \\ b & \gamma \end{pmatrix} \begin{pmatrix} u \\ \omega \end{pmatrix} \tag{7.12}$$

where $\alpha = a + \psi_v$ and $\gamma = c + \psi_\omega$.

This simple propulsion matrix (7.12) contains the basic information of bacterial swimming. It demonstrates that, as $b \neq 0$, a forward velocity u can be generated by the application of an external torque T and that it is only the helical tail that contributes to this coupling. It shows that the forward velocity u is linearly related to the rotational speed ω and, as stated previously, the body does not add to the propulsion but instead decreases the velocity slope (see Fig. 7.5D).

7.3.3 Fabrication of artificial bacterial microrobots

When engineering bacterial microrobots, it would be very difficult to replicate the molecular motor design of bacteria. As we will see in Section 7.4, the use of rotating magnetic fields to externally power the microrobots removes the need for an on-board motor and bearing between the helical tail and the body. Instead, the focus lies on the challenging fabrication of three-dimensional helix structures at the microscale. Three methods for the fabrication of helical structures will be given special attention in this section, as they produce micrometer-scale robots in a controllable and repeatable manner. What they have in common is that they produce microrobots that have a helical shape mimicking the bacterial flagella, which is why bacterial microrobots are often referred to as ABFs. The other common design parameter is the use of magnetic material in some form or another, which is essential for the magnetic actuation.

7.3.3.1 Self-scrolling method

The self-scrolling technique was the first method published capable of controllable batch fabrication of bacterial microrobots [31–34]. The technique is based on a thin film deposition onto a sacrificial layer using molecular beam epitaxy. Structures are patterned with a lithography and a subsequent reactive ion etching (RIE) step. After removing the sacrificial layer, the remaining thin film structures roll up due to internal stresses in the material (see Fig. 7.6A). The rolling direction is preferred along the ⟨001⟩ direction of the wafer. By choosing the alignment angle between the rolling direction and the ribbon pattern, the helicity angle can be chosen precisely. The radius of the helix is controlled by the thickness of the thin-film layer. Common materials are Si or GaAs composites, which are not magnetic. A magnetic material, for example nickel, is therefore deposited at one end of the ribbon before the self-scrolling step. Using soft magnetic material requires the shape of the magnetic material to be designed such that it has an easy axis of magnetization perpendicular to the helical axis.

7.3.3.2 GLAD method

The glancing angle deposition (GLAD) uses vacuum deposition onto a substrate at an oblique angle combined with a controlled motion of the stage holding the substrate [35]. In standard thin film deposition, the atoms strike the surface at an angle of 90°. If the substrate is tilted, the atoms agglomerate at nucleation sites, and the material is only deposited along the "line-of-sight" resulting in gaps between the nucleation sites and in pillars growing in the direction of the vapor flow. By a slow and steady rotation of the stage, these pillars are grown into helical shapes (see Fig. 7.6B). This method results in very densely packed batch fabrication of helical swimmers. Similar to the self-scrolling ABFs, a magnetic material has to be deposited onto the GLAD grown helices in a second step. This is performed by first releasing the structures by sonication and evaporating cobalt on the helices laid flat on a surface. Unlike the

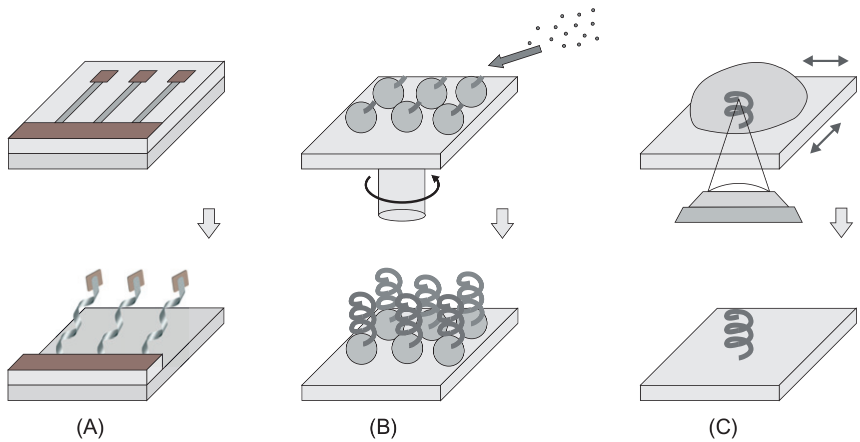

FIGURE 7.6

Fabrication methods. (A) Self-scrolling technique. After the patterned thin-film deposition, the sacrificial layer is removed and the ribbons curl into helices. (B) GLAD method. Vapor deposition at an oblique angle creates pillars growing from the nucleation sites. Rotation of stage results in helical filaments. (C) 3D lithography. Polymerization of photocurable liquid at the laser focal point. Movement of the stage allows the fabrication of arbitrary shapes.

self-scrolled ABFs that have magnetic material only at one end and with a defined shape, the GLAD grown helices have a magnetic film along the whole structure. For magnetic actuation, the magnetization has to be perpendicular to the helical axis, which is achieved by permanently magnetizing the cobalt in the last fabrication step.

7.3.3.3 3D lithography method

The previous methods used fabrication techniques designed for 2D structures in such a way that the 3-dimensional helices could be created. In recent years, commercial machines have become available that allow 3D lithographic patterning of photosensitive polymers. A 2-photon polymerization occurs at the focal point of the laser and, combined with a motorized stage, true 3D structures can be achieved with high flexibility in terms of shapes and sizes (see Fig. 7.6C). A major drawback is the fact that it is not a batch fabrication process. Also, the combination of multiple materials and compatibility with other fabrication methods remain a challenge. One way to circumvent an additional step of magnetic material deposition is to use a magnetic particle polymer composite. Microstructures have successfully been written using ferromagnetic particles embedded in the photocurable polymer. One possibility is to permanently magnetize the particles in the polymer perpendicular to the helical structures [36, 37].

7.4 Actuation of artificial bacterial microrobots

Bacterial microrobots swim by rotating around their helical axis which creates a forward propulsion; i.e., along their helical axis. Unlike *E. coli* bacteria, which use an on-board rotary motor to rotate their flagella, bacterial microrobots have no relative motion between their helical tail and body and the rotation of the whole microrobot, i.e., body and tail simultaneously, is achieved by a wireless application of a magnetic torque.

7.4.1 Magnetic forces and torques

We use the term *magnetic body* for objects consisting of material that is either permanently magnetized or material that is magnetized when subjected to an external magnetic field. The force $\boldsymbol{F}_m$ and torque $\boldsymbol{T}_m$ on a magnetic body with volume V in an external magnetic field $\boldsymbol{H}$ $[\mathrm{A \cdot m^{-1}}]$ are

$$\boldsymbol{F}_m = \mu_0 V (\boldsymbol{M} \cdot \nabla) \boldsymbol{H} \tag{7.13}$$

$$\boldsymbol{T}_m = \mu_0 V \boldsymbol{M} \times \boldsymbol{H} \tag{7.14}$$

where $\mu_0 = 4\pi \times 10^{-7}\,\mathrm{T \cdot m \cdot A^{-1}}$ is the permeability of free space and $\boldsymbol{M}$ is the magnetization $[\mathrm{A \cdot m^{-1}}]$. For a permanent magnet, the magnetization is a constant value but for soft-magnetic material it is a function of the applied field.

What we can see from these equations is that in a uniform field, i.e., where there are no field gradients, there is no force on a magnetic body and only the magnetic torque acts to align the body's axis of magnetization with the direction of the external field. If a microrobot is put in such a field it will align itself to the field and stop moving as soon as the angle between its magnetization $\boldsymbol{M}$ and the field $\boldsymbol{H}$ becomes zero. In order to keep rotating the microrobot, the external field has to be rotated continuously. The misalignment angle ϕ between the magnetization and the field remains constant, while the rotational speed of the field vector is kept at a constant speed. If the rotational speed changes, the misalignment angle changes as well so that the magnetic torque is in equilibrium with the drag torque acting on the microswimmer. As we showed in Section 7.2, this equilibrium state is reached almost instantaneously.

The microrobot is not only actuated but also steered using magnetic torques. The orientation of the bacterial robot with regard to the world frame is commonly described with a pitch and a yaw angle (see Fig. 7.7). While swimming straight, the external field is rotated in a plane perpendicular to the helical axis. To change the orientation of the swimmer, the plane of rotation is simply deviated until it is perpendicular to the new direction of motion and a steering torque is induced until the artificial swimmer is aligned again. The propulsion and steering torque are not independent; one torque is largest whenever the other one is smallest. This trade-off between simultaneous propulsion and steering can easily be found (see Fig. 7.8A), unless swimming at maximum velocity is attempted. A different way to change the motion direction by 180° is to simply reverse the rotating direction of the field (see Fig. 7.8B).

Uniform rotating magnetic fields are sufficient to actuate and steer bacterial microrobots. Non-uniformities in the applied field, i.e., field gradients, lead to forces acting on the microrobot, which can be seen from Eq. (7.13). These forces are

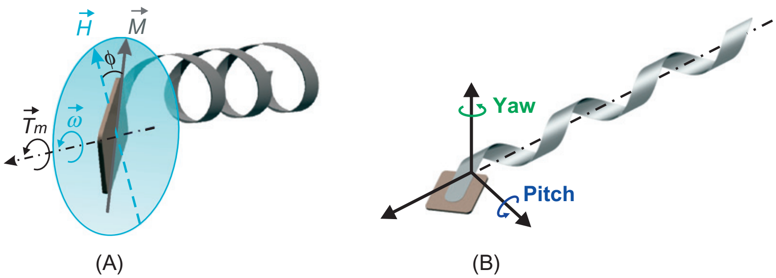

FIGURE 7.7

(A) Application of the magnetic torque. The torque $\boldsymbol{T_m}$ is induced due to the misalignment between the magnetization $\boldsymbol{M}$ of the nickel plate, which is along its diagonal, and the external field vector $\boldsymbol{H}$. The magnetic field vector $\boldsymbol{H}$ is rotated in a plane perpendicular to the helical axis with a rotational speed $\boldsymbol{\omega}$. For a constant rotational speed, the misalignment angle ϕ between $\boldsymbol{M}$ and $\boldsymbol{H}$ is constant (From Ref. [38], © 2010 IEEE). (B) The orientation of the ABF is described by a pitch and yaw angle. Reproduced with permission from Ref. [1], The Royal Society of Chemistry.

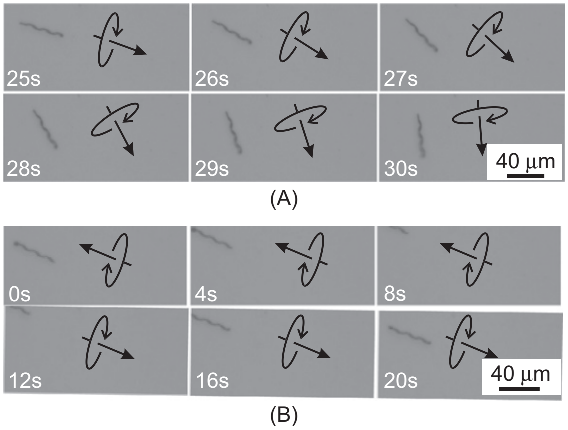

FIGURE 7.8

ABF actuation and steering. (A) A rotational magnetic field is generated which creates a torque on the magnetic body of the microrobot. The ABF is steered by changing the rotational plane of the magnetic field vector. Simultaneous steering and propulsion generation is achieved. (B) The motion can be reversed by changing the rotational direction of the magnetic field. Reprinted with permission from Ref. [33], © 2009 AIP.

generally avoided as the microrobots may get pulled away from the desired motion trajectory. If applied in a controlled manner, however, they could be used as additional degrees of freedom in the actuation of bacterial microrobots, for example to compensate for gravity.

7.4.2 Magnetic field generation

An external magnetic field can either be generated by electromagnetic coils or by a strong permanent magnet. We know additionally that the field vector has to be rotated to apply a constant torque. The following two methods have successfully been employed to actuate artificial bacterial microrobots.

7.4.2.1 *Helmholtz coils*

By running electric current through a coil, a magnetic field is generated. The field strength changes linearly with the current run through the coil. This field is not uniform, as its strength decreases with distance to the coil. A region of almost uniform field can be achieved, however, by placing two identical coils opposite to each other at a distance of R, where R is the radius of the coils. The current should run in the same direction as indicated in Fig. 7.9A. A pair of coils in this configuration are called a *Helmholtz* coil pair. In this way, non-uniformities become negligible in the central workspace between the two coils, and the field only exerts a torque on the swimmer. The most elegant way to generate a rotating field is to use three Helmholtz coil pairs

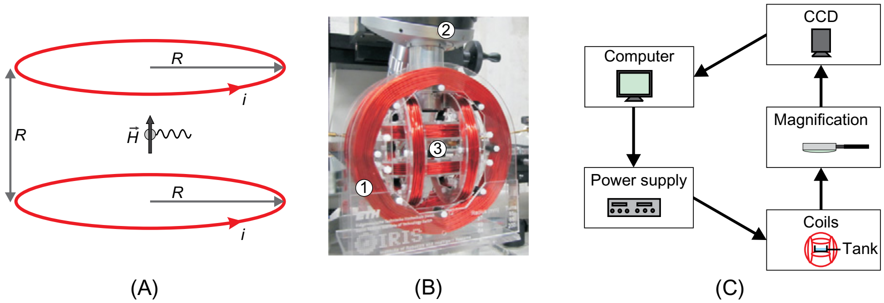

FIGURE 7.9

Electromagnetic setup. (A) Helmholtz coils. Two identical coils with radii R placed at a distance of R from each other produce an almost uniform field in the middle, i.e., along the coil axes at a distance of $R/2$ from each coil. (B) Experimental setup. 1. Three orthogonal Helmholtz coil pairs; 2. microscope lens; 3. central workspace and location of the tank. (C) Schematic of the experimental setup. A swim tank is placed in the middle of the three orthogonal coil pairs. The three coil pairs surrounding the central workspace have different radii in order to physically fit around the central workspace. If the bacterial swimmers are smaller than a few micrometers, the use of a fluorescence microscope is advantageous. The current output is coordinated with a computer and either manual steering or closed-loop control is possible if a visual tracker is employed.

placed orthogonally to each other (see Fig. 7.9B). The field strength and orientation is the summation of the three field vectors of each coil pair and can be chosen arbitrarily by setting the three current inputs independently. Figure 7.9C shows the components of a complete microrobotic setup, including the electromagnetic coils, amplifiers, and optical components, such as a microscope lens and CCD camera, for visual feedback.

7.4.2.2 *Rotating permanent magnet*

Triaxial Helmholtz coil systems are particularly useful for controlling magnetically actuated microrobots due to the fact that they generate only pure magnetic torque with negligible applied magnetic forces. To achieve this property, however, the coils in each pair of the Helmholtz arrangement must be separated by their radius and the microrobot must be operated in the system's common center. If a triaxial Helmholtz coil system is to be used for medical applications, the radius of the smallest coil must be at least large enough to contain the patient with the area of interest positioned in the coil center. While performing surgical procedures on the eye, for example, where the patient lies on his back with his head placed in coil center, the actual diameter of the smallest coil must be at least twice the diameter of his head to keep the position of the eye in the absolute center of the coils.

Helmholtz coils are practical for bench-top applications where the operational workspace of a microrobot in the center of the coils may be several centimeters in size. As the coil sizes increase, the magnitude of the current required to obtain the same magnetic field strength in the workspace center increases proportionally with the coils' radii. Scaling these systems to the size needed for medical applications where a human torso or head may be placed in the center of the Helmholtz coils' operational workspace is hindered by the cooling and infrastructure necessary to accommodate increasing current. Rather than using uniform fields generated by Helmholtz coils, it has been proposed to use non-uniform fields emanating from a single permanent magnet to actuate microswimmers [39]. For clinical applications, a single permanent magnet may be positioned close to the patient, permitting the use of smaller and less expensive systems to achieve the same magnetic field strength—ultimately resulting in systems that scale better for in vivo devices. The fact that magnetic fields generated by permanent magnets are non-uniform and produce an applied force on the microrobot, however, significantly complicates control.

The field **H** generated by a permanent magnet with dipole moment **Γ** at a position in space **p** relative to the center of the permanent magnet is approximated by the point-dipole matrix equation

$$\mathbf{H} = \frac{\mu_0}{4\pi\,|\mathbf{p}|^3}\left[\frac{3\mathbf{p}\mathbf{p}^T}{|\mathbf{p}|^2} - \mathbf{I}\right]\boldsymbol{\Gamma} \tag{7.15}$$

where μ_0 is the constant representing permeability of free space, and **I** is the 3×3 identity matrix. Equation (7.15) is nearly exact for permanent magnets with spherical geometries and is an approximation for the field produced by those with non-spherical geometry. In Ref. [39], the authors find that the point-dipole model closely matches the magnetic field of cylindrical permanent magnets (25.4 mm diameter, 25.4 mm height) magnetized both axially and diametrically (see Fig. 7.10) for distances away from the magnet center greater than 30 mm. In practice, diametrically magnetized cylindrical permanent magnets are particularly well suited for generating the rotating magnetic fields required to actuate helical microswimmers because they (1) completely utilize the volume of the magnet's housing (Fig. 7.10) and (2) their moment area of inertia is less compared to a magnet of the same magnetized volume polarized axially.

7.5 Swimming behavior

From the propulsion matrix Eq. (7.12), we expect that artificial bacterial microrobots swim faster as the rotational frequency increases and that this relationship should be linear. Experiments with currently available microrobots show different swim behavior depending on the proximity to solid boundaries, the frequency of actuation, and under the influence of additional forces, such as gravity or magnetic forces. These phenomena will be addressed in the following sections.

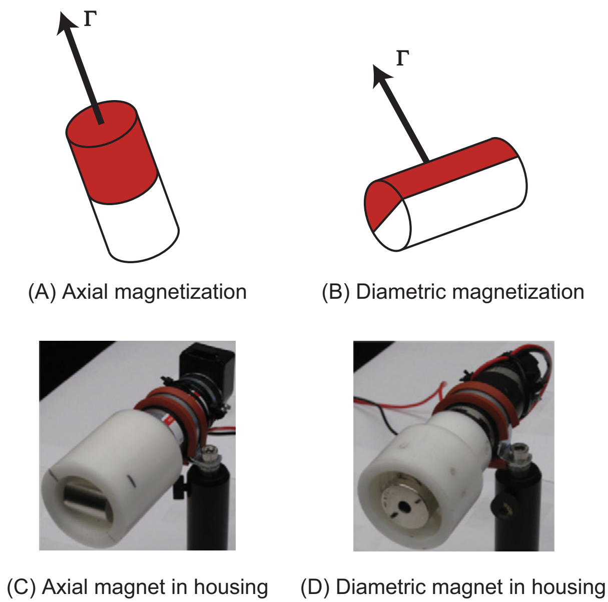

FIGURE 7.10

Rotating permanent magnets polarized axially (A) and diametrically (B) placed in a Delrin housing and mounted to a motor shown in (C) and (D), respectively. Both magnets shown in (C) and (D) are 25.4 mm in diameter and height. In practice, diametric permanent magnets utilize available space more efficiently than axially polarized magnets: the diametric magnet shown in (D) can be increased in size by 50% in the magnetization direction without altering the size of the housing [39].

7.5.1 Overview

Figure 7.11 shows the velocity of an artificial bacterial microrobot near a solid surface at different frequencies of the rotating magnetic field. The total velocity of the microswimmer is separated into a forward velocity u_f, along the direction of the helical axis, and into a drift velocity u_d, perpendicular to the helical axis. The drift angle φ refers to the angle of misalignment between the total velocity and the desired forward velocity. Three characteristic regions can be distinguished in the frequency–velocity plot. The largest middle-range-frequency region is the *linear region*, where the behavior follows the simple propulsion matrix model. Here, we focus on the two extreme regions of very low (*drift-dominated region*) and very high (*step-out region*) frequency.

7.5.2 Drift and wobbling

Until now we have assumed that free-swimming bacterial microrobots have neglected wall effects. At low Reynolds numbers, however, wall effects play a major role

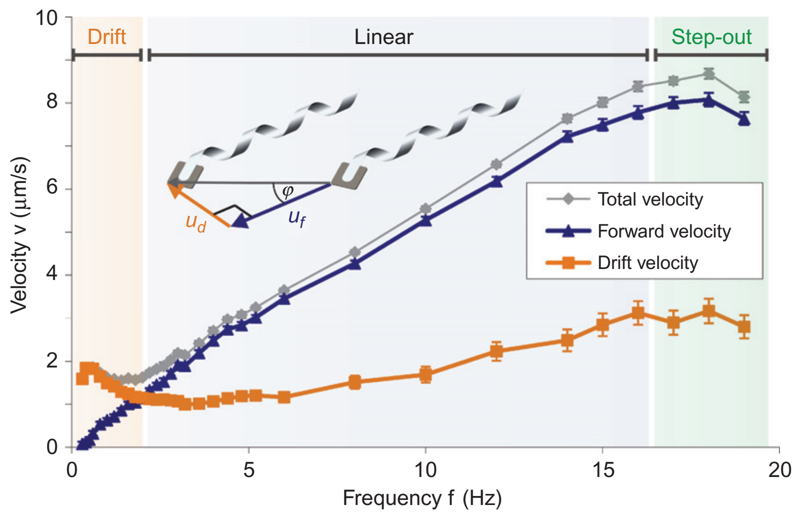

FIGURE 7.11

Velocity of bacterial microrobot versus input frequency. There are three characteristic regions: the *linear region* at middle-ranged frequencies, the *step-out region* at high frequencies, and the *drift-dominated region* at very low frequencies. From Ref. [38], © 2010 IEEE.

and have been observed not only on microrobots but also on living microorganisms [40, 41]. Wall effects are directly responsible for the drifting of microswimmers. Wobbling at low Reynolds number has only been reported for artificial bacterial microrobots [38]. It transpires that the combination of the wall effects and wobbling causes the phenomenon observed in the *drift-dominated region*.

7.5.2.1 Drift

Drag forces encountered by a microswimmer near a solid boundary are non-uniform and increase with proximity to the wall. This results in a drag imbalance between the part of the swimmer that is closer and the part further away from the surface. If we consider a bacterial swimmer, the local drag coefficients along the helical filament become functions of the distance h to the wall $\xi = \xi(h)$. From Fig. 7.12, it can be seen that a filament segment of the helical tail closer to the wall encounters a higher drag than a segment further away. This causes the helix to roll along the surface perpendicular to the helical axis.

The influence of solid boundaries has been observed and analyzed for *E. coli* bacteria [8, 41]. The bacteria swim in circles due to the counter-rotation of their head and helical tail. The ABF has no such counter-rotation and is stabilized with the magnetic steering torque to keep its orientation while it is drifting (Fig. 7.13). The rolling speed increases linearly with the input frequency as does the forward speed.

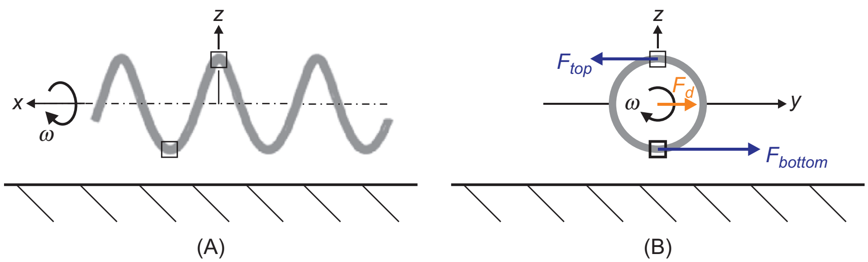

FIGURE 7.12

Wall effects on the ABF. Side view (A) and front view (B) of a helix rotating near a planar wall. Due to the drag force imbalance $F_d = F_{bottom} - F_{top}$ on the tail segments while rotating around the x-axis, the ABF rolls along the surface in the y-direction [38].

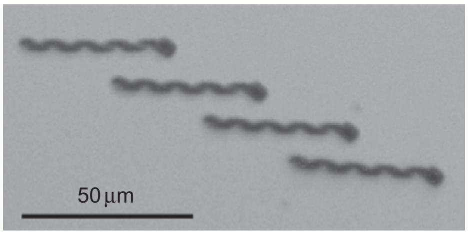

FIGURE 7.13

Time-lapse image showing the top view of an ABF drifting (downward in image) as it swims from left to right. Reprinted with permission from Ref. [34], © 2009 ACS.

This leads to a stable drift angle φ for high frequencies. In the drift-dominated region, a new phenomenon occurs which causes the drift angle to change.

7.5.2.2 Wobbling

At low frequencies, the helical swimmer starts to wobble with increasing precession angle as the frequency goes toward zero [38]. The helical shape of the filament causes a drag torque also perpendicular to the helical axis, which affects the axis of the swimmer and causes precession. Other effects are likely to aggravate non-ideal swimming, such as an imbalance due to gravitational forces or an actuation torque that is not applied along the helical axis. This can occur if the magnetization is not perfectly perpendicular to the helical axis. At high frequency, the precession is attenuated because the total drag on the swimmer is minimized if it rotates around the long body axis, which corresponds to the helical axis (see Fig. 7.14).

7.5.2.3 Combined drifting and wobbling

The reason for the increase in the drift angle lies in the increased efficiency of the side-wise propulsion when the ABF wobbles (see Fig. 7.15). This is due to the increased drag force difference on the filament segments at the bottom and at the top

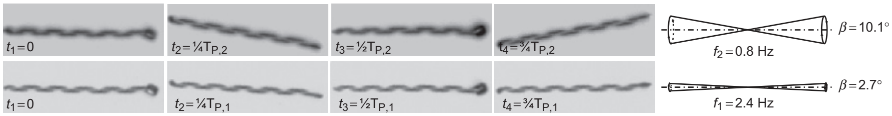

FIGURE 7.14

Time-lapse of the ABF swimming at two different input frequencies $f_2 > f_1$. The frequency of the precession is equal to the input frequency. The precession angle β decreases rapidly for higher frequencies. From Ref. [38], © 2010 IEEE.

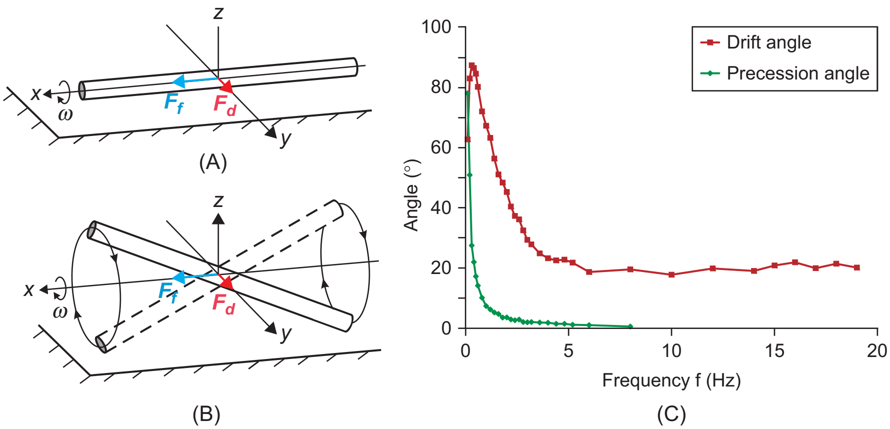

FIGURE 7.15

Schematic showing the rotation of a slender body without (A) and with (B) precession. The slender cylinder is representative of a helical tail. The forward propulsion is decreased with the wobbling while the drifting is enhanced. (C) Experimental results showing the connection between precession and drift decrease. Even for negligible precession motion drifting remains (with an approximately constant drift angle) when in proximity to a wall. From Ref. [38], © 2010 IEEE.

of the helical tail as the distance between the segments grows. While the screw-type swimming becomes less efficient because of the precession motion, the ABF propels itself along the wall, in a manner that resembles a paddling motion, which becomes more efficient as the precession angle increases. The propulsion due to paddling is so effective that the total velocity grows despite the decrease of the input frequency, and a local maximum is reached before the velocity goes to zero (see *drift-dominated region* in Fig. 7.11). The effectiveness of paddling was demonstrated in an experiment inside a microchannel. The image series in Fig. 7.16 show an ABF swimming along the channel (downward in images), and the schematic below shows the lateral position in the channel. At a high frequency, the precession is small, and the swimmer drifts only slightly to the left. At a lower frequency, the side-wise paddling propulsion is strong enough to roll upward along the channel walls onto the flat surface. This

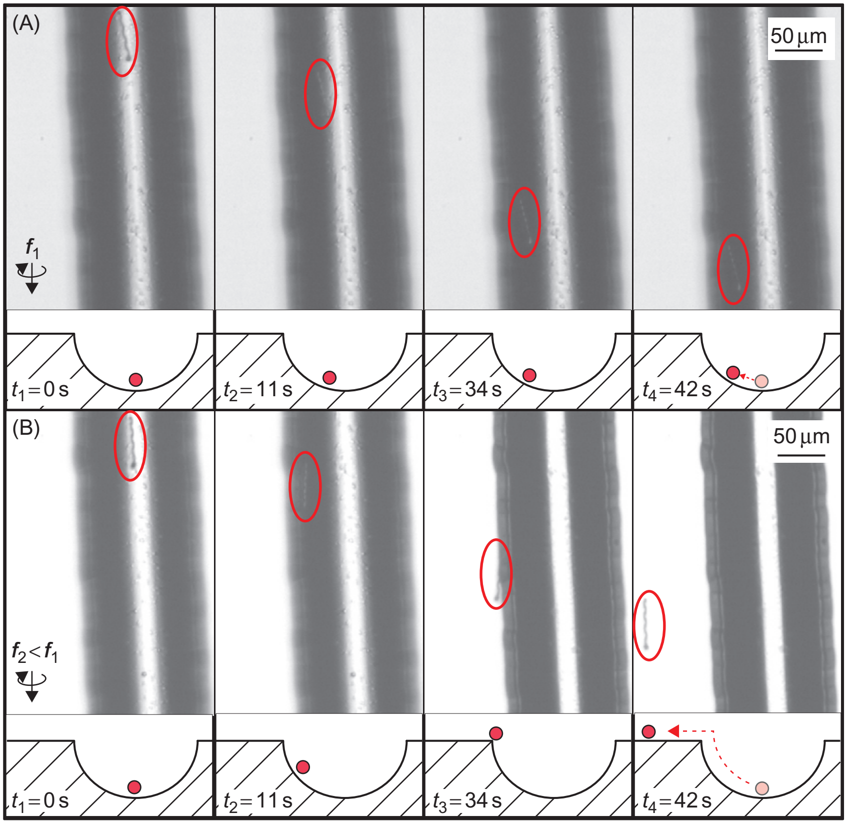

FIGURE 7.16

Time-lapse images of an ABF inside a microchannel. The channel cross section is round and has the dimensions 130 μm (width) × 55 μm (depth). The schematic insets indicate the lateral position of the ABF in the channel. (A) The ABF prototype swims along the channel (downward in image) and exhibits a slight drifting to the left. (B) For a lower frequency, the ABF wobbles and the sidewise propulsion is large enough for the ABF to climb out of the channel. From Ref. [38], © 2010 IEEE.

experiment demonstrates that the wobbling at low frequency in combination with a nearby wall causes strong drifting that is not negligible and which must be accounted for in servoing tasks.

7.5.3 Step-out frequency

The step-out frequency occurs when the drag on the microrobot, which increases with angular and translational velocity, grows larger than the maximum magnetic torque available [42]. At that point, the agent can no longer follow the rotation of the field,

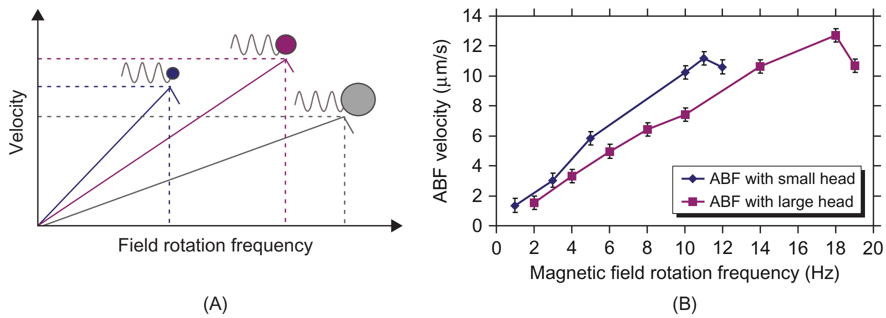

FIGURE 7.17

Step-out frequency for different microrobotic prototypes. (A) Schematic frequency-velocity plot showing the decrease of velocity at the step-out frequency. An increase in the volume of the magnetic material (represented with a larger spherical body) always increases the step-out frequency but, due to increased fluidic drag, not necessarily the maximum velocity [34, 38]. (B) Experimental result showing different step-out frequencies for a small-headed and a large-headed ABF. Material reprinted with permission from Ref. [34], © 2009 ACS.

and it steps out of sync with the external magnetic field vector. From the propulsion matrix, we can see that this limiting frequency ω_{max} is linearly dependent on the magnitude of the maximum magnetic torque that can be conveyed.

$$\omega_{max} = \left(\frac{\alpha}{\alpha\gamma - b^2} \right) \cdot T_{max} \tag{7.16}$$

Equation (7.16) is derived from Eq. (7.10) and is valid for a free swimming microrobot, where $F = 0$. From the magnetic torque in Eq. (7.14), it is apparent that the maximum torque can be amplified by increasing the magnetic field strength or by increasing the volume of the magnetic body [34]. During operation, the field strength is adjusted either by regulating the amount of current through the electromagnetic coils or by changing the distance of the external permanent magnet to the microrobot. Increasing the volume of the magnetic material is (in most cases) equivalent to increasing the total volume of the microrobot (in Fig. 7.17 represented by a larger head), and therefore, additional drag forces are created on the swimmer. Even though the step-out frequency is increased, this is not necessarily the case for the maximum velocity. It has been shown that an optimal trade-off between torque maximization and drag minimization can be found [34, 38].

7.5.4 Gravity compensation

Because man-made microswimmers are typically heavier than their fluid medium, they tend to slowly sink due to their own weight, unlike the bacteria they are designed to mimic which are approximately neutrally buoyant. When swimming under an optical microscope with a small depth-of-field, small changes in the microswimmer's distance from the microscope lens due to drift caused by gravity quickly make the microswimmer to deviate from the focal plane. This downward drift can be counteracted by pitching the microswimmer upward and increasing the rotational frequency accordingly to obtain the desired velocity (see Fig. 7.18). There is a unique combination of pitch angle and rotational frequency that will cause the microswimmer to swim at a desired velocity provided that the necessary rotational frequency is less than step-out.

How the force due to gravity influences the microswimmer's velocity u in the direction parallel to its principle axis with the microswimmer rotating at frequency ω is described by the propulsion matrix (7.10). For gravity compensation, a relationship between the force $\mathbf{F}$ acting on the microswimmer in any direction to the velocity of the microswimmer $\mathbf{U}$ in any direction with the microswimmer rotating about its principle axis with angular velocity $\boldsymbol{\Omega}$ is needed ($\mathbf{F}$, $\mathbf{U}$, and $\boldsymbol{\Omega}$ are now three-dimensional vectors). The linear equation of interest to the problem of gravity

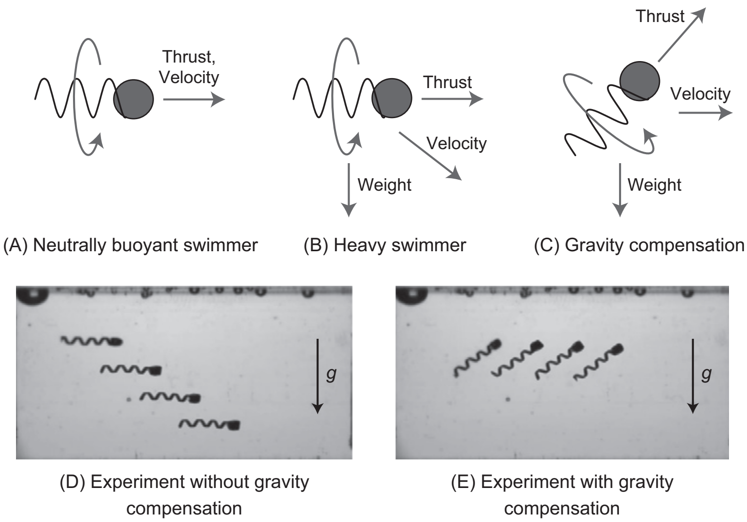

FIGURE 7.18

Flagellated bacteria are nearly neutrally buoyant (A), whereas man-made microswimmers are typically heavier than their fluid medium, causing them to drift downward under their weight (B). This downward drift is compensated for by commanding the microswimmer to swim at a unique pitch angle and rotation frequency (C). (D) and (E) are composite images from experiments where the microswimmer is commanded to move horizontally with a constant velocity, without and with gravity-compensation, demonstrating the behaviors described in (B) and (C), respectively. Used with permission Ref. [29].

compensation relates **F** to **U**, and **Ω**, and is obtained from the 6 × 6 matrix Eq. (7.4):

$$\mathbf{F} = A\mathbf{U} + B\mathbf{\Omega} \tag{7.17}$$

which can be transformed to

$$\mathbf{U} = D\mathbf{F} + E\mathbf{\Omega} \tag{7.18}$$

where $D = A^{-1}$ and $E = -A^{-1}B$ are 3 × 3 matrices expressed in the reference frame of the microswimmer, assigned such that the **x** axis of the swimmer frame is aligned with the principle axis of the microswimmer and the **z** axis lies in the plane shared by **U** and **F** as shown in Fig. 7.19. The modeled coefficients of D and E are found in Ref. [29] using resistive force theory, although in practice they can be determined experimentally (see Ref. [29] for details).

With desired velocity **U** referenced from vertical by the angle α, we define the pitch angle of the microswimmer to be the angle ψ as measured from **U**. For any given **U** and **F**, the angle ψ is found by

$$\psi = \tan^{-1}\left(\frac{d_{33}|\mathbf{F}|\sin(\alpha)}{|\mathbf{U}| + d_{33}|\mathbf{F}|\cos(\alpha)}\right) \tag{7.19}$$

where d_{33} is the third coefficient on the diagonal of matrix D. To obtain the desired velocity **U** given the angle ψ, the microswimmer must operate at the rotational frequency

$$|\mathbf{\Omega}| = \frac{|\mathbf{U}|\cos(\psi) + d_{11}|\mathbf{F}|\cos(\psi - \alpha)}{e_{11}} \tag{7.20}$$

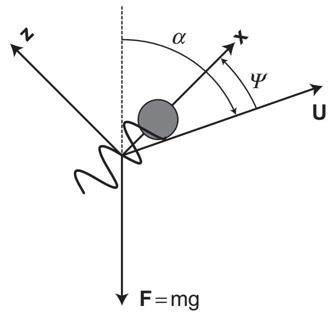

FIGURE 7.19

A microswimmer coordinate frame is assigned such that the **x** axis of the frame is aligned with the principle axis of the microswimmer, and the **z** axis of the frame always lies in the same plane as the desired microswimmer velocity **U** and force due to gravity **F**.

where d_{11} and e_{11} are the first coefficients on the diagonal of the matrices D and E, respectively. The microswimmer can be controlled in an open-loop fashion using these values obtained for ψ and $|\mathbf{\Omega}|$ by ensuring that the rotation axis of the applied magnetic field is pitched above the desired velocity $\mathbf{U}$ by angle ψ and rotates at a frequency of $|\mathbf{\Omega}|$.

To date, microswimmers are typically operated by manually controlling the rotational speed and rotation axis of the applied magnetic field. This is sufficient for simple maneuvers; however, for complex maneuvers that may be required for manipulation or other applications where precision is required, the necessary control inputs for applied field rotation speed and axis may be difficult or nonintuitive for a human operator. The Eqs. (7.19) and (7.20) offer a different paradigm for control where the operator controls the desired velocity $\mathbf{U}$, and the control system uses Eqs. (7.19) and (7.20) to set the rotation speed and pitch angle of the applied field's axis of rotation. Using the input of desired velocity that has both direction and magnitude is more spatially intuitive than controlling the applied field's axis of rotation and speed manually. In Ref. [29], the authors present an open-loop controller based on Eqs. (7.19) and (7.20) enabling maneuvers that would be difficult for an operator to execute if controlling the rotation speed and axis of the applied magnetic field by hand, such as the U-turn maneuver shown in Fig. 7.20. Experiments were conducted using a 6-mm-long helical swimmer immersed in corn syrup, which is dynamically similar (by matching the Reynolds number) to a 140 μm-long microswimmer immersed in water. Without closing a feedback loop, however, the authors show that the open-loop controller tends to be sensitive to variation in the parameters d_{11}, d_{33} and e_{11}, which may fluctuate if the viscosity of the medium changes. These disturbances can be compensated for by the operator if it is perceived that the swimmer is not moving as desired, since correcting Cartesian velocity inputs are more intuitive to a human operator than corrections in pitch and rotation speed.

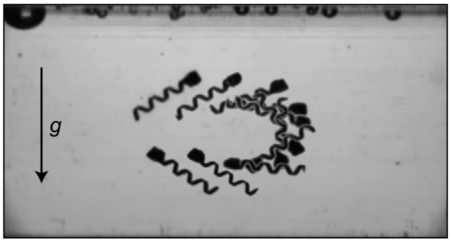

FIGURE 7.20

A U-turn maneuver would be difficult to execute if controlling the rotation speed and rotation axis of the applied magnetic field manually. This maneuver was performed using desired microswimmer velocity **U** as a simple and intuitive input to an open-loop controller based on Eqs. (7.19) and (7.20). Used with permission from Ref. [29].

7.5.5 Break-away and step-out frequencies in non-uniform fields

When using a single permanent magnet to generate rotating applied fields necessary for propulsion, we consider microswimmers to be placed in one of either the *axial control* or *radial control* positions. With world coordinate axis $\{\mathbf{x}, \mathbf{y}, \mathbf{z}\}$ defined and with the actuator permanent magnet lying rotating around the $\mathbf{x}$ axis in the $\mathbf{y}$-$\mathbf{z}$ plane, the microswimmer is in the axial control position if the vector $\mathbf{p}$, describing the position of the microswimmer's magnetic moment relative to that of the actuator, lies parallel to the $\mathbf{x}$ axis (Fig. 7.21A). In this position, the magnetic field applied to the microswimmer always points in the opposite direction of the actuator's dipole moment $\mathbf{\Gamma}$, and the field magnitude $|\mathbf{H}|$ varies purely as a function of the microswimmer's distance from the actuator, $|\mathbf{p}|$:

$$|\mathbf{H}| = \frac{\mu_0 |\mathbf{\Gamma}|}{4\pi |\mathbf{p}|^3} \tag{7.21}$$

If the microswimmer is positioned so that the $\mathbf{p}$ lies in the $\mathbf{y}$-$\mathbf{z}$ plane, then the microswimmer is in the radial control position (Fig. 7.21B). In the radial control position, the magnitude of the applied field varies with both $|\boldsymbol{p}|$ and the angle of the actuator's dipole moment $\mathbf{\Gamma}$ measured from the $\mathbf{z}$ axis by angle θ in Fig. 7.21:

$$|\mathbf{H}| = \frac{\mu_0 |\mathbf{\Gamma}|}{4\pi |\mathbf{p}|^3} \sqrt{1 + 3\cos^2\theta} \tag{7.22}$$

Compared to the field magnitude in the axial position, the magnitude in the radial position ranges over one revolution of θ from 100% to 200% of the magnitude in

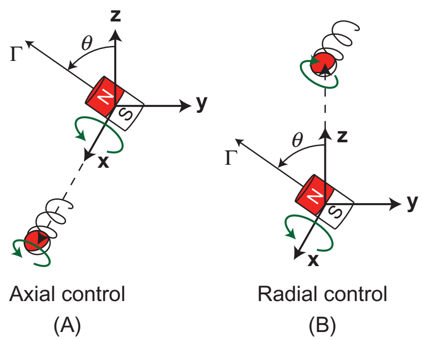

FIGURE 7.21

The microswimmer is in the axial control position (A) when placed purely along the **x** world axis. When the microswimmer lies in the **y**-**z** plane, it is said to be in the radial control position (B).

the axial position for the same $|\mathbf{p}|$. Unlike axial control, the applied magnetic field direction in the radial position is no longer opposite the actuator's dipole moment and is described by $\beta = \tan^{-1}(\tan(\theta)/2)$, where β is measured from the $\mathbf{z}$ axis in the same manner as θ. Because both the magnitude and direction of the applied field fluctuate with the orientation of the actuator, analysis in the radial control position is significantly more complex than axial control. Therefore, our discussion of actuating microswimmers using rotating permanent magnets is limited to control in the axial position.

The applied magnetic force acting on the helical microswimmer by the actuator dipole field $\mathbf{H}$ is given by Eq. (7.13) in both the axial and radial positions. If we denote the dipole moment of the magnetic body rigidly attached to the microswimmer by $\mathbf{M}$ with volume V, then Eq. (7.13) can be expressed as

$$\mathbf{F}_m = \mu_0 V(\mathbf{M}\cdot\nabla)\mathbf{H} = \mu_0 V \begin{bmatrix} \frac{\partial}{\partial x}\mathbf{H}^T \\ \frac{\partial}{\partial y}\mathbf{H}^T \\ \frac{\partial}{\partial z}\mathbf{H}^T \end{bmatrix} \mathbf{M} \tag{7.23}$$

In the axial control position, with ϕ measuring the lead angle between the applied field $\mathbf{H}$ and the microswimmer's dipole moment $\mathbf{M}$ (as shown in Fig. 7.7), the applied magnetic force has magnitude

$$F_m = \frac{3\mu_0 V|\mathbf{\Gamma}||\mathbf{M}|}{4\pi|\mathbf{p}|^4}\cos\phi \tag{7.24}$$

and acts in the negative $\mathbf{x}$ direction, pulling the microswimmer toward the actuator. If the microswimmer is swimming toward the actuator, then the applied magnetic force contributes to the microswimmer's forward velocity according to the swimmer's propulsion matrix (7.12). If the microswimmer is swimming away from the actuator, then the magnetic force tends to attract the swimmer opposite the direction of forward motion. In this case, in order to travel away from the actuator, the microswimmer must be rotated fast enough for the generated fluidic force to overcome the attractive magnetic force. The rotation frequency where the fluidic force balances the magnetic force is referred to as the *break-away* frequency and is given by

$$\omega_{break} = \frac{3\mu_0 V|\mathbf{\Gamma}||\mathbf{M}|}{4\pi|\mathbf{p}|^3}\frac{1}{\sqrt{(|\mathbf{p}|b)^2 + (3\gamma)^2}} \tag{7.25}$$

where the elements of the microswimmer's propulsion matrix (7.12), b and γ, describe how the microrobot's rotation frequency is related to fluidic force and magnetic torque, respectively.

For viable propulsion, the microswimmer must be rotated faster than the break-away frequency while remaining slower than the step-out frequency. At any given time, the rotation frequency of the microswimmer is a function of the applied magnetic force and torque and is derived from the microswimmer's propulsion matrix:

$$\omega = \left(\frac{\alpha}{\alpha\gamma - b^2}\right)T - \left(\frac{b}{\alpha\gamma - b^2}\right)F \approx \left(\frac{\alpha}{\alpha\gamma - b^2}\right)T \tag{7.26}$$

The step-out frequency is the maximum value for ω obtainable from Eq. (7.26). In practice, despite the presence of the magnetic force (7.24), we find that the step-out frequency when actuated in the axial position is effectively equivalent to step-out when operating in uniform magnetic fields where no magnetic force is present. This is due to the fact that for typical microswimmers, $b \ll \alpha$ and $F < T$ (numerically) as the distance between the actuator and swimmer increases, making the contribution of the magnetic torque to the step-out frequency (7.26) dominate that from the applied magnetic force. In uniform fields, the lead angle ϕ converges to 90° when driving the microswimmer at its step-out frequency. Operating the microswimmer at this frequency in the axial position also causes ϕ to converge to 90°, and in this configuration, by Eq. (7.24), the applied magnetic force vanishes. This is an important result because when the microswimmer is driven at the step-out frequency, where the magnetic torque is maximized with zero applied magnetic force, the microswimmer behaves as if it were actuated within the uniform field of a Helmholtz coil system.

In Ref. [39], Fountain et al. demonstrated the break-away and step-out frequencies experimentally using a large swimmer, 4.1 mm in diameter and 12.1 mm in length (shown on the bottom of Fig. 7.22B), placed in a water-filled lumen positioned axially to a diametrically magnetized permanent magnet rotated using a motor (shown

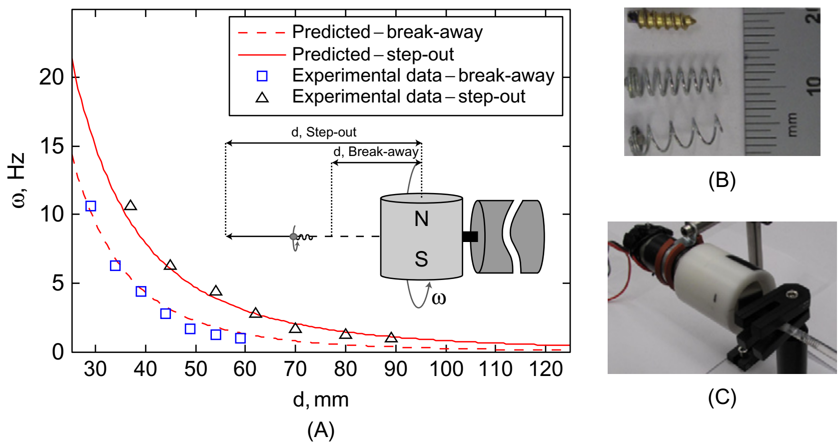

FIGURE 7.22

The break-away and step-out frequencies (A) for the swimmer shown in the bottom of (B) is plotted as a function of the swimmer's distance from the rotating permanent magnet actuator (C) in the axial position [39].

in Fig. 7.22C). The break-away and step-out frequencies are plotted in Fig. 7.22 as a function of the swimmer's distance from the actuator. When rotated at higher frequencies, the swimmer can overcome the attractive magnetic force nearer to the actuator, however, the swimmer tends to step-out closer to the actuator as well. When rotated slowly, the swimmer must be positioned far away from the actuator to break away from the attractive magnetic force, however, the swimmer can travel much farther before it steps out. This is due to the fact that the magnetic force decreases with $|\mathbf{p}|^{-4}$ but the applied magnetic torque, which governs the step-out frequency, decreases an order of magnitude slower with $|\mathbf{p}|^{-3}$.

7.6 Artificial bacterial microrobot in biomedical applications

7.6.1 Current achievements

In this chapter, we have seen the successful fabrication, actuation, and control of artificial bacterial microrobots. These methods summarize the present-day approach to the challenges of microrobot designs, though new methods may emerge in this rather young research area. The investigation of current bacteria-inspired microrobots has led to a number of experimental results and successes in preliminary manipulation tasks and the potential of these microrobots for biomedical applications are discussed in this section.

7.6.1.1 Maneuverability

There are a number of factors that play an important role in achieving 3D motion with microrobots. First, the system has to be capable of generating magnetic fields that are strong enough and can be oriented arbitrarily in 3D. Second, a microrobotic agent has to be fabricated that fulfills a combination of fluid mechanical and magnetic requirements to achieve enough propulsive force to allow it to swim against the gravitation pull. Third, other forces, such as magnetic gradient field forces, have to be overcome as well. Only then true 3D navigation is possible (see Fig. 7.23) and gravity compensation algorithms become necessary. Both actuation approaches presented in this chapter, i.e., electromagnetic coils or rotating permanent magnets, have

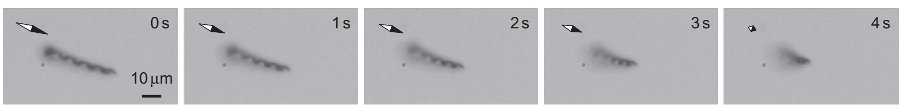

FIGURE 7.23

Artificial bacterial flagellum steered in 3D. Insets (compass needle) indicate the orientation given by the input signal.

achieved the generation of the demanded field strengths. By design, artificial bacterial microrobots are capable of navigating in a range of different environments. They can perform in large cavities as well as within small tubes, both of which are present in the human body. Their motion paths are easily reversed, as they can swim both forwards and backwards simply by changing the direction of field rotation. This would, for example, allow easy extraction from a site by reversing the trajectory. Combining all these characteristics makes the artificial bacterial microrobot a promising microrobot design for biomedical applications.

7.6.1.2 Swarm control

External magnetic field actuation is well suited to moving swarms of bacterial microrobots. Each agent is subject to the same field orientation, and whole groups of agents can be moved simultaneously without any additional energy output of the system (see Fig. 7.24). As these robotic agents are very small, it makes sense to use a multitude of them to, for example, increase the amount of drug delivered to a cancer site. A swarm of microswimmers may also be easier to detect because they can emit a stronger signal as a group, for example in the form of fluorescence brightness.

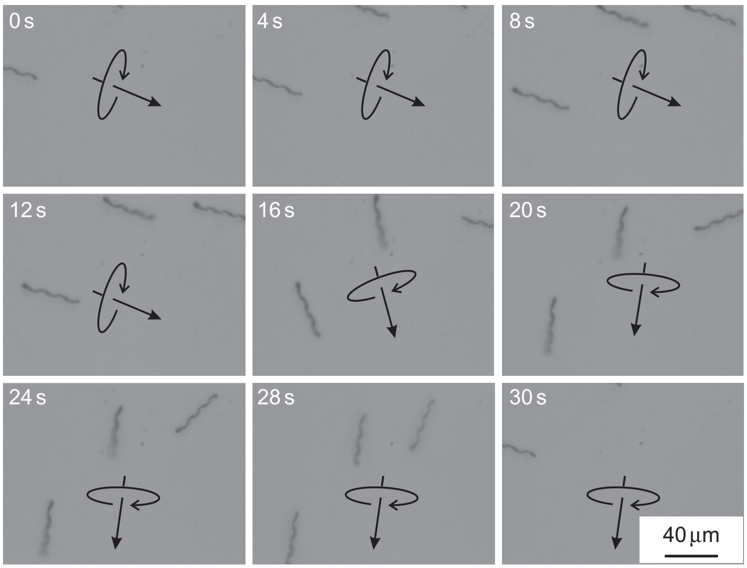

FIGURE 7.24

Swarm-like behavior of three ABFs controlled as a single entity with the input command indicated by the arrows. During a relatively abrupt steering movement, one ABF is temporarily separated from the group, but it naturally rejoins. Reprinted with permission from Ref. [34], © 2009 ACS.

7.6.1.3 Micromanipulation

Manipulation tasks at the microscale range from pushing, rotating, and twisting to probing of and injecting into living organisms (see Fig. 7.24). The most obvious way to manipulate microbeads may be by pushing and rotating the beads. For controlled long-distance transport it would be necessary to fabricate robot designs that allow confinement of the cargo. A more efficient way of transporting multiple beads is by pumping them with the flow field generated by the swimming microagent. The transport is enhanced by the presence of a nearby boundary which enables unilateral displacement of the microbeads. If this method was used on living cells, it would additionally ensure the safety of the organism as no contact between the microrobot and the cells occurs. These preliminary results show the feasibility of these types of manipulation tasks for *in vitro* experiments handling and investigating cells.

7.6.2 Outlook

There are a number of challenges that remain to be addressed with regard to the design of complete microrobotic systems. First, the tracking of microrobots in vivo remains a mostly unresolved issue. While current approaches rely on visual feedback,

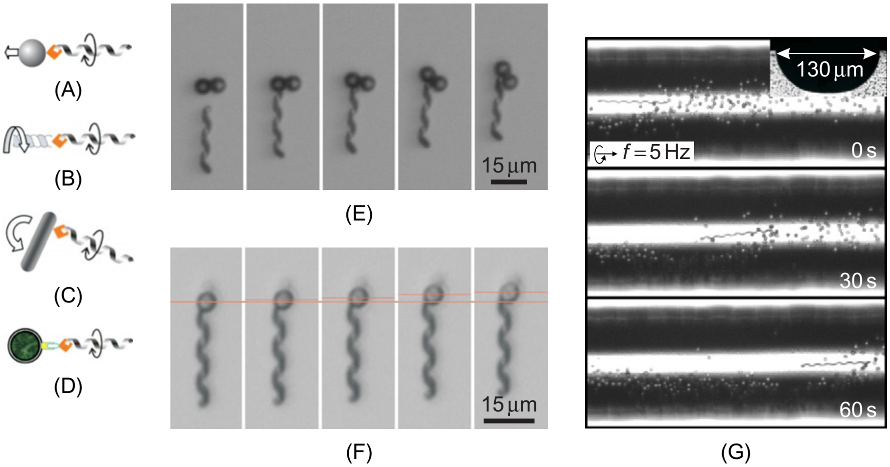

FIGURE 7.25

Micromanipulation with artificial bacterial microrobots. (A)–(D) Conceptual view of contact manipulatin tasks (© 2009 IEEE [43]). (E) Two polystyrene microspheres are rotated 70º by an ABF pushing on one of the microspheres. The optical microscope image sequence represents 2 s of elapsed time. (F) A microsphere is pushed for a radius length by an ABF within 1 s. Images (e) and (f) are reprinted with permission [33], © 2009 AIP. (G) Manipulation of 3 μm beads inside a channel. Due to the proximity to the of the surface the beads are moved unilaterally (downwards in image). Reproduced with permission from Ref. [1], The Royal Society of Chemistry.

usually by microscopes for magnification and CCD cameras for image caption, new tracking methods are required for the guidance of microagents inside the human body. Second, new materials have to be explored that are biocompatible or even bioerodible. Yet the inclusion of magnetic metals cannot be avoided, and, therefore, non-toxic coatings have to be used or magnetic particles have to be embedded securely within the material. Surface coatings are necessary not only for encapsulating material but can also play an essential role in the functionality of the microrobot. For example, the microrobot can be coated by smart materials for sensing or for controlled drug loading and release.

References

[1] Zhang L, Peyer KE, Nelson BJ. Artificial bacterial flagella for micromanipulation. Lab chip 2010;10(17):2203–15.

[2] Purcell EM. Life at low reynolds number. Am J Phys 1977;45(1):3–11.

[3] Normand T, Lauga E. Flapping motion and force generation in a viscoelastic fluid. Phys Rev E 2008;78(6):061907.

[4] Happel J, Brenner H. Low Reynolds number hydrodynamics with special applications to particulate media. Englewood Cliffs, NJ: Prentice-Hall, Inc.; 1965.

[5] Ludwig W. Zur theorie der flimmerbewegung (dynamik, nutzeffekt, energiebilanz). J Comp Physiol A-Neuroethol Sens Neural Behav Physiol 1930;13(3):397–504.

[6] Hancock GJ. The self-propulsion of microscopic organisms through liquids Proc R Soc Lond A 1953;217(1128):96–121.

[7] Youngren GK, Acrivos A. Stokes flow past a particle of arbitrary shape: a numerical method of solution. J Fluid Mech 1975;69:377–403.

[8] Lauga E, Powers TR. The hydrodynamics of swimming microorganisms Rep Prog Phys 2009;72:096601.

[9] Pozrikidis C. Introduction to theoretical and computational fluid dynamics. New York: Oxford University Press; 1997.

[10] Young D, Chiu C, Fan C, Tsai C, Lin Y. Method of fundamental solutions for multidimensional Stokes equations by the dual-potential formulation. Eur J Mech B-Fluids 2006;25(6):877–93.

[11] Tran-Cong T, Phan-Tien N. Boundary element solution for half-space elasticity or strokes problem with a no slip boundary Comput Mech 1986;1:259–68.

[12] Phan-Tien N, Tran-Cong T, Ramia M. A boundary element analysis of flagellar propulsion. J Fluid Mech 1987;1184:533–49.

[13] Muldowney GP, Higdon JJ. A spectral boundary element approach to three-dimensional stokes flow. J Fluid Mech 1995;298:167–92.

[14] Fujita T, Kawai T. Optimum shape of a flagellated microorganism. Trans Jpn Soc Mech Eng 2001;67:753–8.

[15] Goto T, Masuda S, Terada K, Takano Y. Comparison between obwervation and boundary element analysis of bacterium swimming motion. Trans Jpn Soc Mech Eng 2001;67:330–5.

[16] Ishikawa T, Sekiya G, Imai Y, Yamaguchi T. Hydrodynamic interactions between two swimming bacteria. Biophys J 2007;93:2217–25.

[17] Cortez R. The method of regularized stokeslets. SIAM J Sci Comput 2001;23(4):1204–25.
[18] Cortez R, Fauci L, Medovikov A. The method of regularized stokeslets in three dimensions: analysis, validation, and application to helical swimming. Phys Fluids 2005;17:031504.
[19] Batchelor GK. Slender-body theory for particles of arbitrary cross-section. J Fluid Mech 1970;44:419–40.
[20] Johnson RE. An improved slender-body theory for stokes flow. J Fluid Mech 1980;99:411–31.
[21] de Mestre, NJ, Russel WB. Low-reynolds-number translation of a slender cylinder near a plane wall. J Eng Math 1975;9(2):81–91.
[22] Cox RG. The motion of long slender bodies in a viscous fluid part 1. general theory. J Fluid Mech 1970;44:791–810.
[23] Kim M, Powers TR. Hydrodynamic interactions between rotating helices. Phys Rev E 2004;69:061910.
[24] Smith DJ, Gaffney EA, Blake JR. Discrete cilia modelling with singularity distributions: application to the embryonic node and the airway surface liquid. Bull Math Biol 2007;69:1477–510.
[25] Chwang AT, Wu TY. A note on helical movement of micro-organisms. Proc R Soc Lond B 1971;178(1052):237–346.
[26] Lighthill J. Flagellar hydrodynamics. SIAM Rev 1976;18(2):161–230.
[27] Berg HC, Anderson R. Bacteria swim by rotating their flagellar filaments. Nature 1973;245:380–2.
[28] Berg H. The rotary motor of bacterial flagella. Annu Rev Biochem 2003;72:19–54.
[29] Mahoney AW, Sarrazin JC, Bamberg E, Abbott JJ. Velocity control with gravity compensation for magnetic helical microswimmers. Adv Robot 2011;25(8):1007–28.
[30] Purcell EM. The efficiency of propulsion by a rotating flagellum. Proc Natl Acad Sci USA 1997;94(21):11 307–11.
[31] Bell DJ, Leutenegger S, Hammar KM, Dong LX, Nelson BJ. Flagella-like propulsion for microrobots using a nanocoil and a rotating electromagnetic field In: Proc. IEEE Int. Conf. Robotics and Automation; 2007. p. 1128–33.
[32] Bell DJ, Bauert TE, Zhang L, Dong LX, Sun Y, Grützmacher D, et al. Directed batch assembly of three-dimensional helical nanobelts through angular winding and electroplating. Nanotechnology 2007;18(5):055304.
[33] Zhang L, Abbott JJ, Dong LX, Kratochvil BE, Bell DJ, Nelson BJ. Artificial bacterial flagella: fabrication and magnetic control. Appl Phys Lett 2009;94:064107.
[34] Zhang L, Abbott JJ, Dong LX, Peyer KE, Kratochvil BE, Zhang HX, et al. Characterizing the swimming properties of artificial bacterial flagella. Nano Lett 2009;9(10):3663–7.
[35] Ghosh A, Fischer P. Controlled propulsion of artificial magnetic nanostructured propellers. Nano Lett 2009;9(6):2243–5.
[36] Kobayashi K, Ikuta K. Three-dimensional magnetic microstructures fabricated by microstereolithography. Appl Phys Lett 2008;92(26):262505.
[37] Xia H, Wang J, Tian Y, Chen Q-D, Du X-B, Zhang Y-L, et al. Ferrofluids for fabrication of remotely controllable micro-nanomachines by two-photon polymerization. Adv Mater 2010;22(29):3204–7.

[38] Peyer K, Zhang L, Kratochvil B, Nelson B. Hallo non-ideal swimming of artificial bacterial flagella near a surface. In: Proc. IEEE Int. Conf. Robotics and Automation, 2010. p. 96–101.
[39] Fountain T, Kailat P, Abbott J. Wireless control of magnetic helical microrobots using a rotating-permanent-magnet manipulator. In: Proc. IEEE Int. Conf. Robotics and Actuation, 2010. p. 576–81.
[40] DiLuzio WR, Turner L, Mayer M, Garstecki P, Weibel DB, Berg H.C, et al. Escherichia coli swim on the right-hand side. Nature 2005;435(7046):1271–4.
[41] E, DiLuzio WR, Whitesides GM, Stone HA. Swimming in circles: motion of bacteria near solid boundaries. Rep Prog Phys 2006;90:400–12.
[42] Abbott JJ, Peyer KE, Lagomarsino MC, Zhang L, Dong LX, Kaliakatsos IK, et al. How should microrobots swim? Int J Robot Res 2009;28(11–12):1434–47.
[43] Zhang L, Abbott JJ, Dong LX, Kratochvil BE, Zhang H, Peyer KE, et al. Micromanipulation using artificial bacterial flagella. In: IEEE/RSJ Int. Conf. Intelligent Robots and Systems, 2009. p. 1401–6.